International Journal of Heat and Mass Transfer 208 (2023) 124059

Contents lists available at ScienceDirect

International Journal of Heat and Mass Transfer

journal homepage: www.elsevier.com/locate/hmt

Dependency of transition in thermocapillary convection on volume ratio in annular pools of large-*Pr* fluid in microgravity

Ziyi Guo[1,2], Jicheng Li[3], Kai Li[1,2,*], Jianfu Zhao[1,2], Wenrui Hu[1,2]

[1] National Microgravity Laboratory, Institute of Mechanics, Chinese Academy of Sciences, Beijing 100190, China
[2] School of Engineering Science, University of Chinese Academy of Sciences, Beijing 100149, China
[3] School of Energy and Power Engineering, Lanzhou University of Technology, Lanzhou 730050, China

ARTICLE INFO

Article history:
Received 1 January 2023
Revised 14 February 2023
Accepted 6 March 2023
Available online 21 March 2023

Keywords:
Thermocapillary convection
Microgravity
Annular pool
Transitions
Dynamic mode decomposition

ABSTRACT

Thermocapillary convection driven by the horizontal temperature gradient is a typical nonlinear dynamical system. As the applied temperature difference increases, the flow undergoes a series of transitions into turbulence. Volume ratio of the liquid layer *Vr* (liquid volume/volume of the container) is a critical parameter that affects transition behaviors of the convection. Direct numerical simulations on thermocapillary convection in annular liquid pools with various volume ratios are carried out. Characteristics of the oscillatory convection are detected by time series and frequency spectrum analyses. The dynamic mode decomposition (DMD) method is also adopted to investigate inherent structures of the flow field. Effect of *Vr* on oscillation characteristics under a wide range of temperature differences from 10K to 90K is discussed. Results show that in annular pools with lager volume ratios, the thermocapillary convection is chaotic under very large ΔT and its transition behaviors are more complicated.

1. Introduction

The most intensively studied convection in space is the fluid flow driven by the horizontal surface tension gradient [1]. Under normal gravity, convection is driven by both buoyancy and thermocapillary force, while in microgravity environment the buoyancy effect is suppressed. Previous works clarified that thermocapillary convection shows various flow patterns under different temperature gradients, such as steady, asymmetric, oscillatory, and turbulent states, and therefore it is significant to expand the theoretical frameworks to understand the dynamical mechanisms of the thermocapillary convection [1].

Annular layers are a typical model that stimulates the interest of the scientific community by virtue of its elimination of the sidewalls in the azimuthal direction [1]. This feature supports the investigation of the property and waveforms of the supercritical hydrothermal waves. The critical and supercritical transitions of thermocapillary convection in annular pool are heavily dependent on fluid properties, geometry configurations, thermal boundary conditions, etc. Schwabe et al. [2,3] carried out the microgravity experiment MAGIA to study thermocapillary flow structures without coupling the buoyancy flow in annular layers of different depths heated at the outer wall and cooled at the inner wall. They investigated the multi-roll-states of thermocapillary convection under different Prandtl numbers and aspect ratios. Schwabe and Benz [4] reported experimental results of thermocapillary flow in an annular pool with an adjustable depth h, $2.5 \leq h \leq 20$ mm. They identified hydrothermal waves for small h and more complicated oscillations for larger h. They also measured the critical Marangoni number for different aspect ratios Ar ($= \Delta r/h$). Recently, Kang et al. [5–7] conducted a series of space experiments using an annular liquid pool on board the China's SJ-10 recovery satellite. They investigated effects of the free-surface shape on the stability of thermocapillary convection. Dynamics and transitions of the wave pattern were observed and nonlinear dynamics of travelling waves, standing waves, and counter-propagating waves were also studied. In addition to space experiments, many numerical studies on annular layers have been reported in the past two decades. Using linear stability analysis, Hoyas et al. [8] obtained the stability diagram for the flow in annular pools of silicone oil heated at the inner wall. By numerical simulations, Sim et al. [9] showed that heat loss through the interface increases critical Reynolds number and decreases critical frequency in an annular pool heated at the outer wall. Shi and Imaishi [10] determined critical conditions for the onset of oscillatory flows in a shallow annular pool of silicone oil of $Pr = 6.7$. Liu et al. [11] conducted linear stability analysis on thermocapillary convection in annular liquid layers of silicon melt ($Pr = 0.011$) with the meniscus surface, and they investigated ef-

* Corresponding author.
E-mail address: likai@imech.ac.cn (K. Li).

https://doi.org/10.1016/j.ijheatmasstransfer.2023.124059
0017-9310/

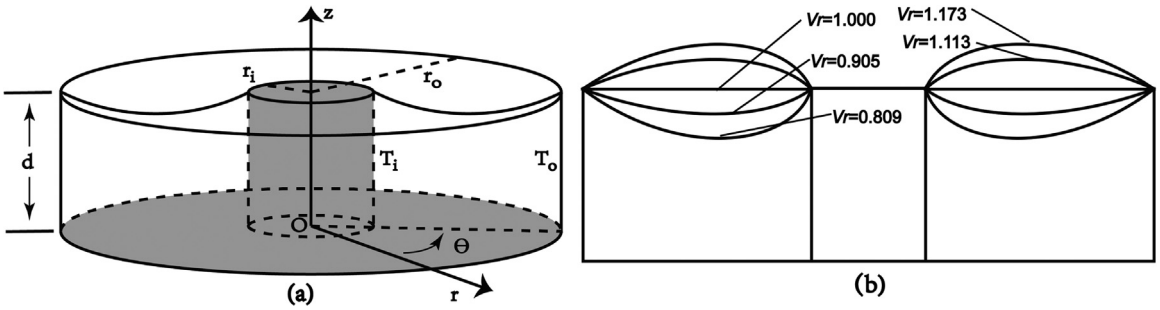

Figure 1. Physical model: (a) sketch of the annular pool; (b) free surface configurations of liquid layer with Vr = 0.809, 0.905, 1.000, 1.113, 1.173.

fect of the volume ratio Vr on the stability limit of steady thermocapillary flow. They clarified the relationship between the critical Marangoni number and the volume ratio.

Chaos is a state which is enormously complex and unpredictable for long times, even if the underlying dynamical system is deterministic. Chaos has been observed in many natural nonlinear processes. Typical routes by which systems transition from regular to irregular motion have been identified. Gollub and Benson [12] conducted terrestrial experiments on buoyancy convection and found Rulle-Takens route, Feigenbaum route and Manneville–Pomeau route to chaos. Bucchignani and Mansutti [13] numerically studied 3D buoyant-thermocapillary convection in a cavity, and they showed evidence that the system evolves to chaos following the Ruelle-Takens route. Li et al. [14] conducted direct numerical simulations on 2D thermocapillary convection in a rectangular cavity, and they found that the flow takes different routes (quasi-periodic and period-doubling routes) to chaos for different aspect ratios. Zhang et al. [15] numerically investigated bifurcation routes to chaos of thermocapillary convection in an annular pool; they also found different routes for different Biot number.

Influence of volume ratios on thermocapillary convection in annular pools is still an open question, and most of the works focuses on critical stage at which the convection loses stability [5–7]. In our previous work [16], dependency of critical values of thermocapillary convection in annular pools of large-Pr fluid on volume ratios has been studied. In this work, simulations under much larger Marangoni numbers (ΔT) are conducted to investigate dependency of supercritical transitions on volume ratios. The physical model and fluid property chosen here are identical to those of the space experiment in China's SJ-10 recovery satellite [5–7].

Velocity and temperature fields of the thermocapillary convection are calculated using direct numerical simulations (DNS), and characteristics of transitions are obtained using time series analysis and dynamic mode decomposition (DMD). This paper is organized as follows: physical and mathematical models are introduced in section 2, numerical aspects of the simulations are described in section 3, section 4 is about the results and discussions, and finally the conclusions are given in section 5.

2. Physical and mathematical model

Figure 1 shows the annular liquid pool and free surface configurations of the liquid layer with different volume ratios. Radius of the inner wall is r_i = 4mm, and of the outer wall is r_o = 20mm. The gap width is defined as $\Delta r = r_o$-r_i, and height of the pool is d = 12mm. The inner wall is heated at T_i, and the outer wall is cooled at T_o = 290K. The working fluid is 2cSt silicone oil with Pr = 28.01. The volume ratio is defined as $V_r = V_l / (\pi d{r_o}^2 - \pi d{r_i}^2)$, where V_l is the volume of liquid. Simulations of thermocapillary convection in liquid layer with Vr = 0.809, 0.905, 1.000, 1.113 and 1.173 are conducted under different temperature differences ($\Delta T = T_o$-T_i).

The mathematical model is composed of the continuity, momentum and energy equations for the fluid. The dimensionless governing equations can be written as (Einstein's summation convention is implied for repeated indices)

$$\frac{\partial U_i}{\partial X_i} = 0 \tag{1}$$

$$\frac{\partial U_j}{\partial \tau} + \frac{\partial (U_i U_j)}{\partial X_i} - \frac{\partial}{\partial X_i}\left(\frac{\partial U_j}{\partial X_i}\right) = -\frac{\partial P}{\partial X_j} \tag{2}$$

$$\frac{\partial \Theta}{\partial \tau} + \frac{\partial (U_i \Theta)}{\partial X_i} - \frac{1}{Pr}\frac{\partial}{\partial X_i}\left(\frac{\partial \Theta}{\partial X_i}\right) = 0 \tag{3}$$

where X_i denotes the i-th Cartesian coordinate, U_i the i-th Cartesian velocity component, τ the time. In deriving the above equations, the length, velocity, temperature difference (T-T_o), pressure and time are scaled by the reference length, velocity, temperature difference, pressure and time

$$l_{ref} = d,\ u_{ref} = \frac{\nu}{d},\ T_{ref} = T_i - T_o,\ p_{ref} = \rho u_{ref}^2,\ \tau_{ref} = \frac{l_{ref}}{u_{ref}} \tag{4}$$

where p is the pressure, T the fluid temperature, ρ the density, ν the kinematic viscosity, α the thermal diffusivity and $Pr = \nu/\alpha$ the Prandtl number.

3. Numerical aspects

3.1. Numerical methodology

According to the advantages discussed in [17], a block-structured grid [18] with matching/non-overlapping interfaces was adopted in the present study. The domain was divided into more than 30,0000 finite control volumes (CVs). Non-uniform grid assignment is employed in the physical domain to improve the resolution near the boundaries.

Due to the non-orthogonality of the grids and the curvilinear boundaries, the boundary-fitted-coordinate (BFC) method [19] is adopted. The governing equation in the physical space (X_i, i=1,2,3) is first transformed to the computational space (ξ_i, i=1,2,3) and takes the following form after the coordinate transformation:

$$\frac{\partial U_k^*}{\partial \xi_k} = 0 \tag{5}$$

$$\frac{\partial U_j}{\partial \tau} + \frac{1}{J}\frac{\partial (U_k^* U_j)}{\partial \xi_k} - \frac{1}{J}\frac{\partial}{\partial \xi_k}\left(Jg_{kl}\frac{\partial U_j}{\partial \xi_l}\right) = -\frac{\partial P}{\partial \xi_k}\frac{\partial \xi_k}{\partial X_j} \tag{6}$$

$$\frac{\partial \Theta}{\partial \tau} + \frac{1}{J}\frac{\partial (U_k^* \Theta)}{\partial \xi_k} - \frac{1}{PrJ}\frac{\partial}{\partial \xi_k}\left(Jg_{kl}\frac{\partial \Theta}{\partial \xi_l}\right) = 0 \tag{7}$$

where $J = \partial(X_1, X_2, X_3)/\partial(\xi_1, \xi_2, \xi_3)$ is the Jacobian matrix, and $g_{kl} = (\partial \xi_k/\partial X_i)(\partial \xi_1/\partial X_i)$ is the metric tensor. In Eq. (5), U_k^* is the contravariant velocity, which is defined as $U_k^* = (JU_j\ \partial \xi_k)/\partial X_j$.

The shape function is applied to estimate the derivatives related to the coordinate transformation $\partial X_i/\partial \xi_j$, where X_i is expressed as $X_i = \sum_{n=1}^{8} \varphi_n(\xi_1, \xi_2, \xi_3) X_i^n$, i=1, 2, 3, $\varphi_n(\xi_1, \xi_2, \xi_3)$ is the shape function and subscript n denotes the corner points of the CV. This method is found to be able to improve the accuracy of the metric valuables such as the Jacobian matrix and the metric tensor.

Governing equations are discretized using a fully conservative finite-volume method with a non-staggered arrangement of the variables [20]. Central difference is used for all spatial derivatives and first order forward difference for the time derivatives. For the convective term, QUICK scheme [21] is applied. Based on the continuity equation, a pressure-correction equation is derived according to SIMPLE algorithm [22]. To ensure the correct coupling of pressure and velocity fields, the well-known Rhie-Chow interpolation technique [20] is applied. The time interval $\Delta\tau = 10^{-5}$ is tested to be suitable.

The code for handling meniscus shapes is validated in [23], and the validation of this code is also confirmed by previous work [16] on the effect of volume ratio on the critical value.

3.2. Boundary conditions

For curved free surface, detailed dimensionless boundary conditions can be found in [16,23], so only a brief description is given here:

1) The velocity at the free surface is determined by the balance between the thermocapillary force and the shear stress of the fluid, and an important dimensionless parameter, the Marangoni number, is defined as $Ma = -(\gamma_T \Delta T d)/\mu\nu$, where γ_T is the temperature coefficient of surface tension. The free surface is assumed to be adiabatic.
2) The no-slip boundary condition is imposed at the solid walls. The temperature at the inner and outer walls is fixed, and the bottom is assumed to be adiabatic.

The initial velocity of the fluid is 0, and the temperature difference is assumed to be directly applied between the inner and outer walls at the beginning of the calculation ($\tau = 0$). The free surface shape is calculated from the Young-Laplace equation at $\tau = 0$ and is kept constant over time, which means it is not updated at each time step.

3.3. Dynamic mode decomposition (DMD) [24]

The numerical results are analyzed by the dynamic mode decomposition (DMD) to figure out how the higher instabilities proceed. DMD is known as a powerful tool for analyzing the dynamics of nonlinear systems [25]. DMD assumes that the flow state is a superposition of several "modes", which are produced from the original timeseries data, snapshots of the flow fields, and the corresponding eigenvalues determine both the growth (or decay) rates and oscillation frequencies of each mode. In this way, although the real fluid flow is governed by infinite-dimensional partial differential equations, its underlying low-dimensional dynamic behaviors can be captured by the truncated modes.

The essence of DMD method is to approximate the original nonlinear system with the locally linear dynamical system, the dynamics can be modeled as

$$\frac{d\boldsymbol{X}}{dt} = \boldsymbol{A}_c \boldsymbol{X} \tag{8}$$

For discrete-time system sampled every Δt in time, the model is

$$\boldsymbol{X}_{k+1} = \exp(\boldsymbol{A}_c \Delta t)\boldsymbol{X}_k \tag{9}$$

The solution to this system can be expressed in terms of the eigenvalues λ_k and eigenvectors $\boldsymbol{\phi}_k$ of the discrete-time map $\boldsymbol{A} = \exp(\boldsymbol{A}_c \Delta t)$

$$\boldsymbol{X}_k = \Sigma_{j=1}^{r} \boldsymbol{\phi}_j \lambda_j^k b_j = \boldsymbol{\Phi}\boldsymbol{\Lambda}^k \boldsymbol{b} \tag{10}$$

Where the coefficients $\boldsymbol{b}$ are the coordinates of the initial vector $\boldsymbol{X}_1$ in the eigenvector basis, and r is the reduced order.

The DMD algorithm produces a low-rank eigen decomposition of the matrix $\mathbf{A}$ that optimally fits the measured trajectory $\boldsymbol{X}_k$ for k = 1,2, . . ., m (m is the number of snapshots), in a least-square sense so that

$$||\boldsymbol{X}_{k+1} - \boldsymbol{A}\boldsymbol{X}_k||$$

is minimized across all points for k = 1,2, . . ., m−1.

The basic procedure for standard DMD consists of the following steps:

1) A sequence of snapshots of the velocity (temperature) fields are collected from the numerical simulation results. These snapshots of velocity (temperature) fields are arranged into two matrices

$$\boldsymbol{X} = [\boldsymbol{x}_1\ \boldsymbol{x}_2 \ldots \boldsymbol{x}_{m-1}],\ \boldsymbol{X}' = [\boldsymbol{x}_2\ \boldsymbol{x}_3 \ldots \boldsymbol{x}_m]$$

2) The locally linear approximation may be written in terms of these data matrices as

$$\boldsymbol{X}' = \boldsymbol{A}\boldsymbol{X} \tag{11}$$

The best-fit $\boldsymbol{A}$ matrix is given by

$$\boldsymbol{A} = \boldsymbol{X}'\boldsymbol{X}^{+} \tag{12}$$

where $\boldsymbol{X}^{+}$ is the Moore–Penrose pseudoinverse.

1) In practice, considering the large dimension of the system and the much smaller rank of $\boldsymbol{A}$, $\widetilde{\boldsymbol{A}}$ is computed to circumvent the computational load,

$$\widetilde{\boldsymbol{A}} = \boldsymbol{U}^{*}\boldsymbol{A}\boldsymbol{U} = \boldsymbol{U}^{*}\boldsymbol{X}'\boldsymbol{V}\boldsymbol{\Sigma}^{-1} \tag{13}$$

where $\boldsymbol{A} = \boldsymbol{X}'\boldsymbol{V}\boldsymbol{\Sigma}^{-1}\boldsymbol{U}^{*}$ is the Singular Value Decomposition (SVD).

1) Then the characteristic modes of $\boldsymbol{A}$ are given by columns of $\boldsymbol{\Phi}$

$$\boldsymbol{\Phi} = \boldsymbol{X}'\boldsymbol{V}\boldsymbol{\Sigma}^{-1}\boldsymbol{W} \tag{14}$$

where columns of $\boldsymbol{W}$ are eigenvectors of $\widetilde{\boldsymbol{A}}$

In this work, the method is implemented in Python using the PyDMD package [26].

4. Discussion

4.1. Time series analysis

As the applied temperature difference (ΔT) increases, the steady axisymmetric thermocapillary convection loses stability and becomes oscillatory flow. The ΔT under which the flow starts to oscillate is defined as the critical temperature difference (ΔT_c). Since the azimuthal velocity is zero in the steady thermocapillary flow, the presence of azimuthal velocity in the liquid is the most sensitive indicator of the transition from steady flow to oscillatory flow. To investigate spatial characteristics of transition behaviors, time evolutions and the corresponding frequency spectra of the azimuthal velocity at a point right below the free surface are examined. For Vr < 1.000 (Vr = 0.809, 0.905), the oscillation is periodic and the fundamental frequency (f_1) increases as ΔT increases

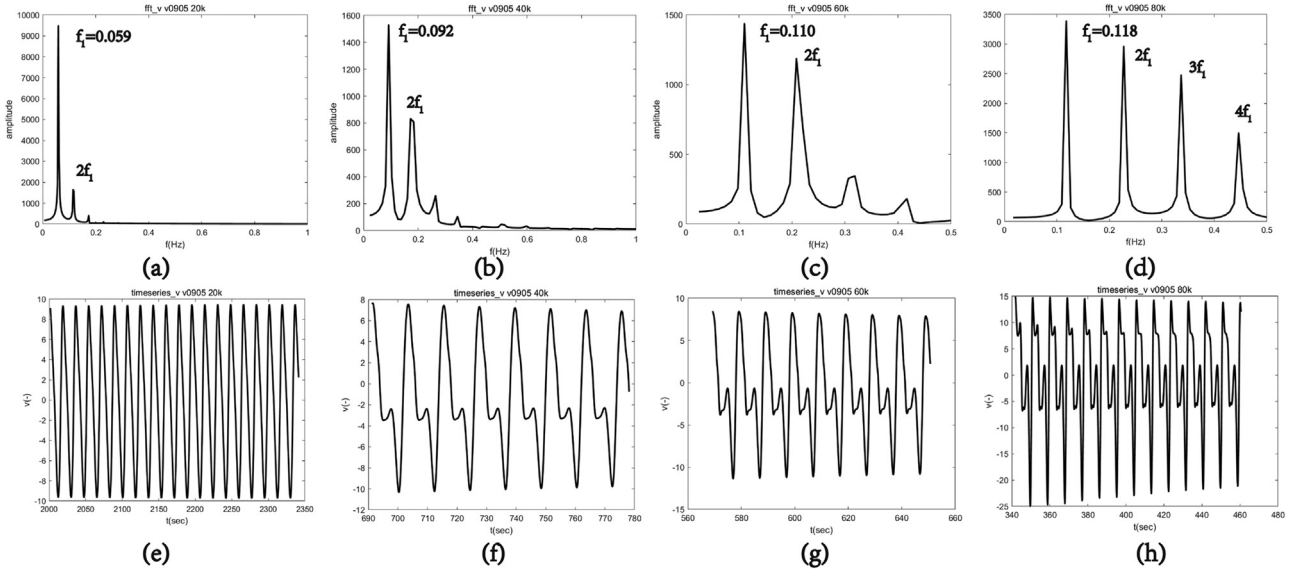

Figure 2. Frequency spectra ((a)∼(d)) and time series ((e)∼(h)) of the azimuthal velocity ($Vr = 0.905$, ΔT = 20K, 40K, 60K, 80K).

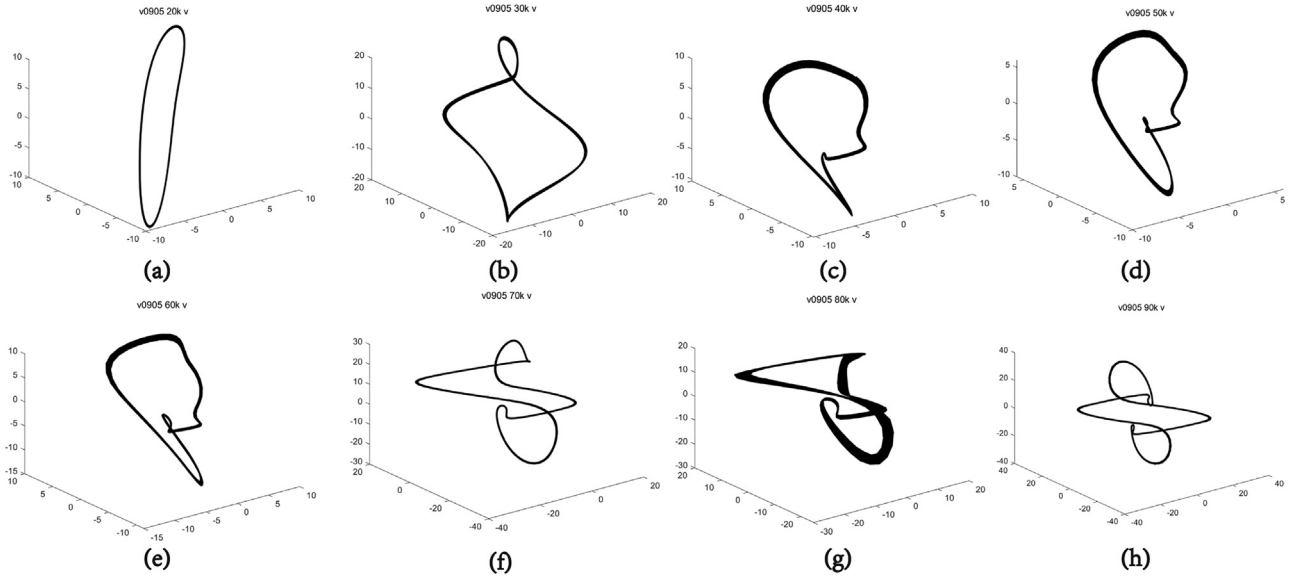

Figure 3. (a)∼(h) Phase space diagrams of the azimuthal velocity time series ($Vr = 0.905$, ΔT = 20K∼90K).

from 20K to 90K. The increase of ΔT leads to the presence of more harmonic frequencies ($2f_1$, $3f_1$,...) in the frequency spectrum (as shown in Figure 2 for $Vr = 0.905$). Using phase space reconstruction, flow dynamics are retrieved from the azimuthal velocity time series. Figure 3 shows phase diagrams of the azimuthal velocity for $Vr = 0.905$ under ΔT from 20K to 90K, and all of them are closed orbits, indicating that flows under these temperature differences are periodic. However, as ΔT increases, the orbit becomes more complex, twisting and folding, and moving away from the simple oval shape. Diversity of the deformed orbit shapes differentiates various flow structures of the periodic flow.

Results for $Vr \geq 1.000$ are different from those for $Vr < 1.000$. In these cases, the time evolution of the azimuthal velocity changes from periodic oscillation to irregular one. As shown in Table 1, for $Vr = 1.000$, the oscillation is periodic under ΔT = 10K and is quasi-periodic with two incommensurate fundamental frequencies under ΔT = 20K to 60K, with three incommensurate fundamental frequencies under ΔT = 70K and 80K. The two frequencies are very close to each other under ΔT = 20K to 40K, while when ΔT reaches 50K and 60K, difference between the two frequencies increases, but under ΔT = 50K, the first fundamental frequency ($f_1 = 0.065$Hz) decreases a little bit. Under ΔT = 90K, the velocity time series is irregular and the power spectrum is continuous (Figure 4). However, several peaks are spaced apart and distinct

Table 1
Frequencies of the azimuthal velocity oscillation ($Vr = 1.000$, ΔT = 20K∼80K).

$\Delta T \setminus f$	f_1	f_2	f_3
10K	0.038		
20K	0.055	0.056	
30K	0.064	0.071	
40K	0.077	0.081	
50K	0.065	0.089	
60K	0.080	0.096	
70K	0.076	0.089	0.100
80K	0.079	0.095	0.108

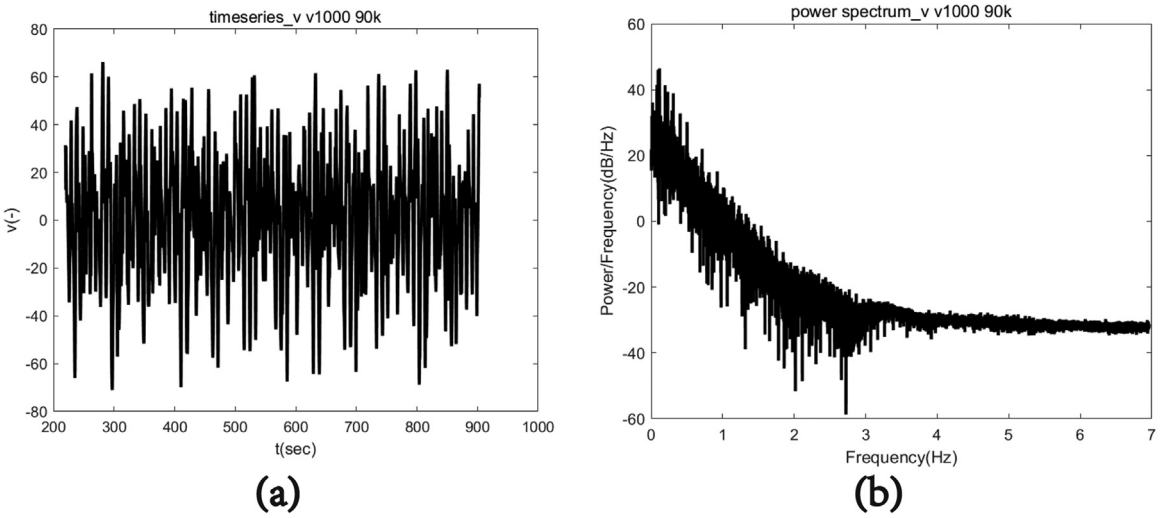

Figure 4. Time series (a) and power spectrum (b) of the azimuthal velocity (Vr = 1.000, ΔT = 90K).

Table 2
Frequencies of the azimuthal velocity oscillation under ΔT = 10K~60K (Vr = 1.113).

$\Delta T \setminus f$	f_1	f_2
10K	0.042	
20K	0.060	
30K	0.066	0.074
40K	0.073	0.084
50K	0.089	
60K	0.085	0.088

Table 3
States of the azimuthal velocity oscillation during the transition (Vr = 0.809, 0.905, 1.000, 1.113, 1.173, ΔT = 10K~90K; S: steady state, P: periodic oscillation, QP: quasi-periodic oscillation, I: irregular, C: chaotic).

$\Delta T/Vr$	0.809	0.905	1.000	1.113	1.173
10K	S	S	P	P	P
20K	P	P	QP	P	P
30K	P	P	QP	QP	QP
40K	P	P	QP	QP	QP
50K	P	P	QP	P	I
60K	P	P	QP	QP	I
70K	P	P	QP	I	C
80K	P	P	QP	C	C
90K	P	P	I	C	C

in the power spectrum (Figure 4b), thus the oscillation is erratic rather than chaotic.

Table 2 and Figure 5 show fundamental frequencies and time series of the azimuthal velocity for Vr = 1.113 under temperature differences from 10K to 60K. When ΔT = 10K and 20K, the oscillation is periodic. Under ΔT = 30K and 40K, the oscillation is quasi-periodic with two fundamental frequencies very close to each other. There are two waves that interfere with each other, and the resulting waveform is a beat, appearing as an envelope in the time series (Figure 5c, d, e). When ΔT = 50K, the oscillation returns to a periodic pattern and shifts to a quasi-periodic pattern once more when ΔT = 60K. As ΔT exceeds 60K, the oscillation becomes irregular. Figure 6 shows power spectra of azimuthal velocity for Vr = 1.113 under ΔT = 70K~90K. The power spectra are continuous and as ΔT increases, the specific peaks do not persist. When ΔT is 80K and 90K, the power spectrum becomes grassy and has many incompletely separated peaks with no obvious pattern of central frequencies and amplitudes, which is the feature of a chaotic signal.

For Vr = 1.173, the oscillation is periodic under ΔT = 10K and 20K, and it is quasi-periodic with two incommensurate fundamental frequencies under ΔT = 30K and 40K. When ΔT exceeds 50K, the time series becomes irregular and the frequency spectrum is increasingly grassy. The flow changes into a chaotic state when ΔT = 70K.

Table 3 summarizes the transition behaviors as ΔT increases, for different values of the volume ratio. For Vr < 1.000, the azimuthal velocity oscillation is always periodic, regardless of ΔT (20K, 30K, …, 90K). For Vr = 1.000, the oscillation changes from a periodic state to a quasi-periodic state and finally to an irregular state as ΔT increases. For Vr > 1.000, the oscillation transitions from a periodic state to a quasi-periodic state and ultimately becomes chaotic. The transition process for Vr = 1.113 is more complicated than that for Vr = 1.173 because the flow undergoes multiple transitions from periodic to quasi-periodic states before it becomes chaotic. Briefly speaking, the larger volume ratio tends to drive flow transition and increase the likelihood of chaotic flow.

4.2. Details of temperature and velocity fluctuations for Vr = 1.113

In the following, more detailed analyses of the transitions of temperature and flow fields in annular pool with Vr = 1.113 will be shown. Vr = 1.113 is chosen because the transition behaviors are most complex as shown in Table 3, i.e., periodic → quasi-periodic → periodic → quasi-periodic → irregular → chaotic. In order to detect the flow and temperature structures, the fluctuation temperature and fluctuation velocity in the azimuthal direction at a fixed position are defined as the dimensionless temperature (velocity) minus its azimuthally averaged value.

4.2.1. Temperature fluctuation field

Figure 7 shows the temperature fluctuation field on the free surface under ΔT = 10K~60K and its spatial-temporal diagram (STD) at dimensionless radial distance R=1.02, where arrows denote the propagation direction of the travelling waves. From the temperature fluctuation field, it is found that the number of waves is 3 in all these cases and the temperature fluctuation is more violent near the inner wall. According to Table 2, under ΔT = 10K, 20K and 50K, the flow is periodic, but the spatial-temporal distributions of their temperature fluctuation fields are quite different

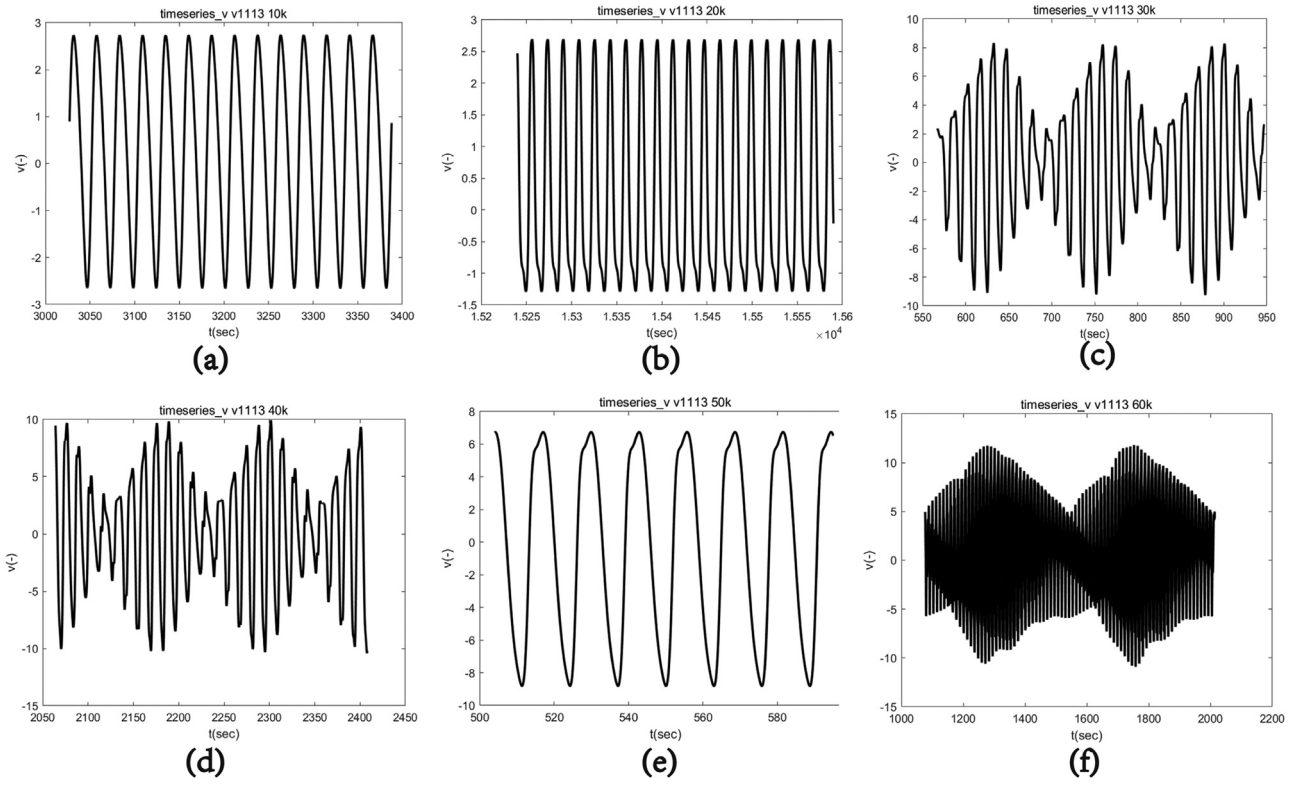

Figure 5. (a)~(f) Time series of the azimuthal velocity under ΔT = 10K~60K (Vr = 1.113).

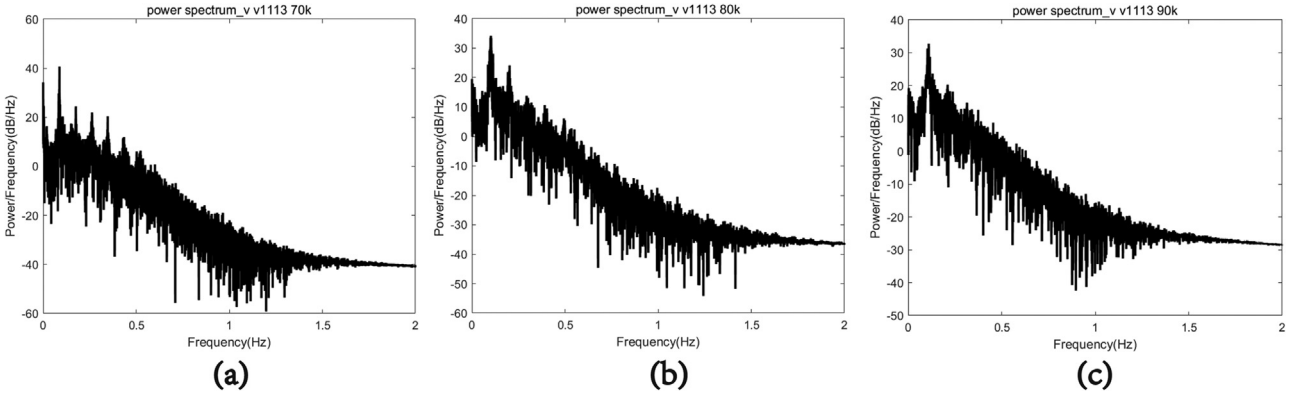

Figure 6. (a)~(c) Power spectra of the azimuthal velocity oscillation under ΔT = 70K~90K (Vr = 1.113).

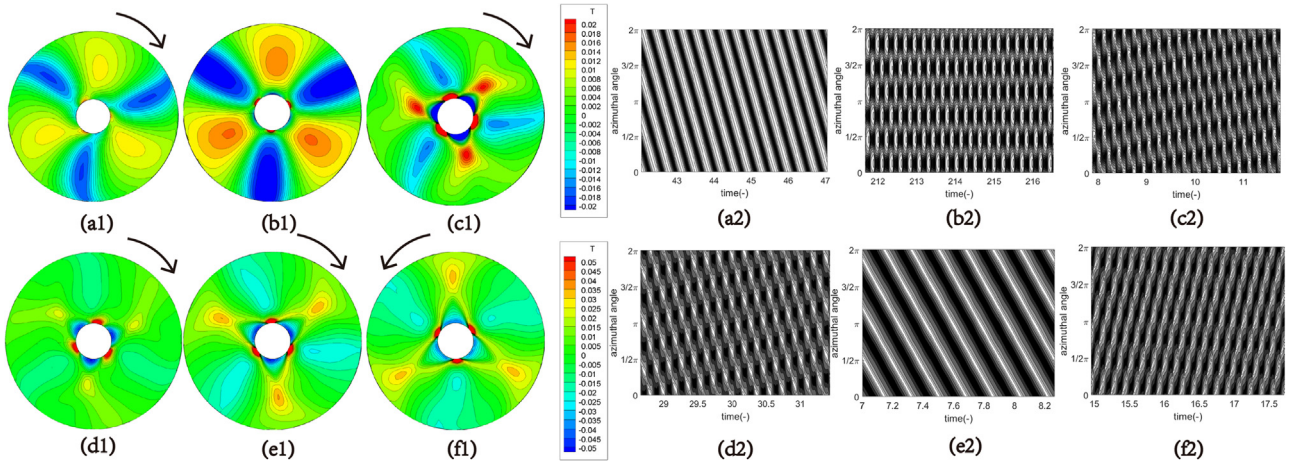

Figure 7. (a1~f1) Temperature fluctuation on the free surface under ΔT = 10K~60K respectively; (a2~f2) STD of the temperature fluctuation at dimensionless radial R=1.02 under ΔT=10K~60K respectively (Vr =1.113).

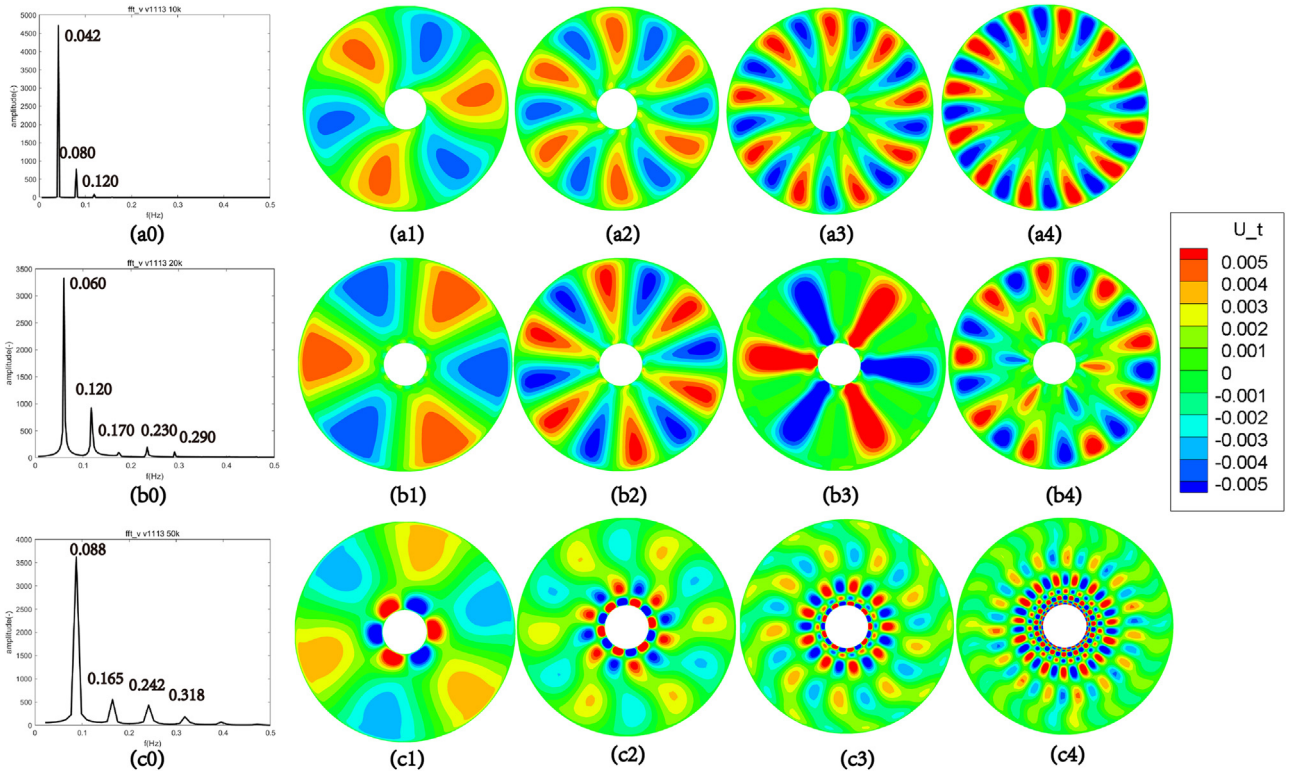

Figure 8. (a0)∼(c0) Frequency spectra of the azimuthal velocity oscillation under ΔT = 10K, 20K, 50K respectively; (a1)∼(a4) four stable azimuthal velocity fluctuation characteristic modes under ΔT = 10K; (b1)∼(b4) four stable azimuthal velocity fluctuation characteristic modes under ΔT = 20K; (c1)∼(c4) four stable azimuthal velocity fluctuation characteristic modes under ΔT = 50K (Vr = 1.113).

and the same is the case when ΔT is 30K, 40K and 60K, under which the flow is quasi-periodic.

When ΔT = 10K and 50K, the oscillation is periodic and the fluctuation propagates along the clockwise direction in a form of a travelling wave. The STD consists of parallel slanted lines (Figure 7a2, e2). When ΔT = 20K, the STD presents as a checkboard-like pattern (Figure 7b2), and in this case the temperature fluctuation field is dominated by the standing wave. The oscillation amplitude is larger under ΔT = 20K than that under ΔT = 10K. When ΔT = 30K, 40K and 60K, the pattern of high and low temperature fluctuations evolves over time in the STD (Figure 7c2, d2, f2), which indicates the presence of both standing wave and travelling wave. Under ΔT = 30K and 40K, the wave propagates in the clockwise direction, while under ΔT = 60K, in the counterclockwise direction. Characteristics of the velocity fluctuation field are similar with those of the temperature fluctuation field.

To summarize, under ΔT = 10K∼60K the sequence of flow transition is: clockwise travelling wave → standing wave → clockwise travelling wave + standing wave → clockwise travelling wave → counterclockwise travelling wave + standing wave. The number of these waves does not change.

4.2.2. Dynamic mode decomposition analysis

To investigate inherent structures of the complex flow fields under large temperature differences, the dynamic mode decomposition (DMD) method is applied. Sequences of velocity and temperature fluctuation fields are collected to construct the snapshot matrix respectively. The reduced order of the truncated modes is 30, in which case the relative error between the reconstructed data and the original data is less than 1%. The dynamic modes can provide insights into both temporal and spatial characteristics of the flow structure, which will be discussed in detail in the following context.

For Vr = 1.113, when ΔT = 10K, 20K and 50K, the oscillation is periodic. Figure 8 shows some of the stable azimuthal velocity fluctuation modes on the free surface under these temperature differences. Frequencies of these modes are 0.040Hz, 0.084Hz, 0.142Hz, 0.230Hz under ΔT = 10K, 0.060Hz, 0.140Hz, 0.293Hz, 0.578Hz under ΔT = 20K and 0.084Hz, 0.230Hz, 0.968Hz, 0.381Hz under ΔT = 50K, which are consistent with frequencies of the flow oscillation (Figure 8a0, b0, c0). When ΔT = 10K and 50K, the travelling wave propagates in clockwise and counterclockwise direction respectively, and as shown in Figure 8a1∼a4, c1∼c4, number of waves of the higher modes is an integer multiple of that of the fundamental mode (mode with the fundamental frequency). However, when ΔT = 20K, number of waves of the third mode is also 3 (Figure 8b3), in which case standing wave takes the place of travelling wave in the azimuthal velocity fluctuation field. Higher modes show the presence of small-scale structures (larger number of wave), which illustrates a scaling between scales of the flow structure and its temporal frequency, indicating a dispersion relation [27].

When ΔT = 30K, 40K and 60K, the oscillation is quasi-periodic. Figure 9 shows some of the stable modes of the azimuthal velocity fluctuation on the free surface under these temperature differences. Frequencies of these modes are 0.067Hz, 0.076Hz under ΔT = 30K, 0.076Hz, 0.087Hz under ΔT = 40K and 0.093Hz, 0.096Hz under ΔT = 60K, which are consistent with the two fundamental frequencies of the flow oscillation (Figure 9a0, b0, c0). Velocity fluctuation fields of the two fundamental modes (modes with frequencies consistent with the fundamental frequencies) have similar structures. The number of waves is 3 and the velocity gradient near the inner wall is larger. However, the wave structure is twisted in the velocity fluctuation field of the second fundamen-

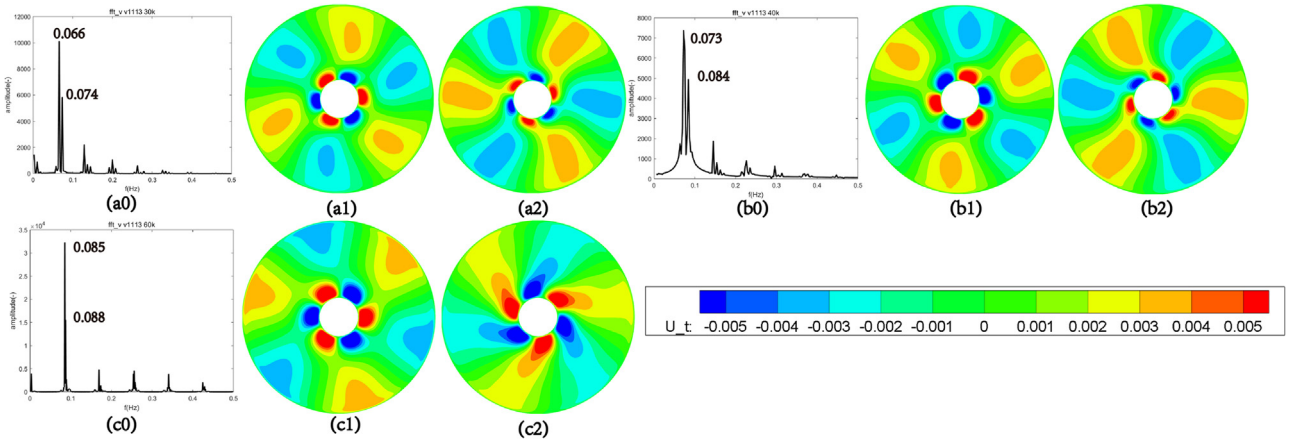

Figure 9. (a0) ∼ (c0) Frequency spectra of the azimuthal velocity oscillation under ΔT = 30K, 40K, 60K respectively; (a1), (a2) two stable azimuthal velocity fluctuation characteristic modes under ΔT = 30K; (b1), (b2) two stable azimuthal velocity fluctuation characteristic modes under ΔT = 40K; (c1), (c2) two stable azimuthal velocity fluctuation characteristic modes under ΔT = 60K (Vr = 1.113).

tal mode. Interactions of the two fundamental modes result in the wave pattern of a mixture of both travelling and standing waves.

In summary, as ΔT increases, spatial and temporal characteristics of the flow has a dramatic change. Generally, under small ΔT, the periodic flow consists of a fundamental characteristic mode and its harmonics, while under larger ΔT, a new characteristic mode with a different fundamental frequency emerges, and the flow oscillation becomes quasi-periodic. Due to the nonlinearity of the thermocapillary convection, the increasing ΔT is not the decisive factor of the occurrence of a new characteristic mode, which can be seen from the fact that the flow transits from quasi-periodic back to periodic state when ΔT increases from 40K to 50K.

5. Conclusion

Thermocapillary convection in annular pools undergoes complicated transitions with the increasing temperature difference, and the transition behaviors are greatly affected by volume ratios of the liquid layer.

For Vr < 1.000, the oscillation is periodic even under very large temperature differences. For Vr = 1.000, the oscillation is periodic under ΔT = 10K, quasi-periodic under ΔT = 20K∼80K, and becomes irregular when ΔT is 90K. For Vr > 1.000, the oscillation changes from periodic to quasi-periodic state as ΔT increases. For Vr = 1.113, the transition process is: periodic → quasi-periodic → periodic → quasi-periodic → irregular → chaotic, while for Vr = 1.173, the process is: periodic → quasi-periodic → irregular → chaotic.

With the DMD method, it is found that periodic flow is characterized by the mode with a fundamental frequency and its harmonics. The number of waves of the harmonic mode is an integer multiple of that of the fundamental mode. Quasi-periodic flow is characterized by modes with different fundamental frequencies. The number of waves of these fundamental modes are the same and flow structures of the modes are quite similar. For Vr < 1.000, since the flow oscillation under all temperature differences is periodic, it seems that contribution of the increasing ΔT is to generate harmonic modes, while for $Vr \geq$ 1.000, the flow transitions to quasi-periodic state from periodic state, so it seems that contribution of the increasing ΔT in this case is to generate different fundamental modes.

In conclusion, liquid layer with smaller volume ratio depresses the generation of new fundamental modes, causing the flow to maintain in a periodic state, while liquid layer with larger volume ratio does not impede the generation of new fundamental modes as ΔT increases, resulting in the flow instability and complex transitions.

Declaration of Competing Interest

The authors declare that they have no known competing financial interests or personal relationships that could have appeared to influence the work reported in this paper.

Data availability

Data will be made available on request.

Acknowledgement

This work was supported by National Key R&D Program of China (Grant No. 2022YFF0503500) and the National Natural Science Foundation of China (Grant No. 11972353). The authors would like to thank Prof. Nobuyuki Imaishi at Kyushu University for his altruistic guides on this article.

References

[1] M. Lappa, Thermal Convection: Patterns, Evolution and Stability, John Wiley & Sons, Ltd, Chichester, UK, 2009, doi:10.1002/9780470749982.
[2] D. Schwabe, A. Cramer, J. Schneider, S. Benz, J. Metzger, Experiments on the multi-roll-structure of thermocapillary flow in side-heated thin liquid layers, Adv. Space Res. 24 (1999) 1367–1373.
[3] D. Schwabe, A. Zebib, B.-C. Sim, Oscillatory thermocapillary convection in open cylindrical annuli. Part 1. Experiments under microgravity, J. Fluid Mech. 491 (2003) 239–258, doi:10.1017/S002211200300541X.
[4] D. Schwabe, S. Benz, Thermocapillary flow instabilities in an annulus under microgravity—Results of the experiment magia, Adv. Space Res. 29 (2002) 629–638.
[5] Q. Kang, D. Wu, L. Duan, J. He, L. Hu, L. Duan, W. Hu, Surface configurations and wave patterns of thermocapillary convection onboard the SJ10 satellite, Phys. Fluids. 31 (2019) 044105.
[6] Q. Kang, J. Wang, L. Duan, Y. Su, J. He, D. Wu, W. Hu, The volume ratio effect on flow patterns and transition processes of thermocapillary convection, J. Fluid Mech. 868 (2019) 560–583.
[7] Q. Kang, H. Jiang, L. Duan, C. Zhang, W.R. Hu, The critical condition and oscillation–transition characteristics of thermocapillary convection in the space experiment on SJ-10 satellite, Int. J. Heat Mass Transf. 135 (2019) 479–490.
[8] S. Hoyas, H. Herrero, A. Mancho, Bifurcation diversity of dynamic thermocapillary liquid layers, Phys. Rev. E. 66 (2002) 057301.
[9] B.C. Sim, A. Zebib, D. Schwabe, Oscillatory thermocapillary convection in open cylindrical annuli. Part 2. Simulations, J. Fluid Mech. 491 (2003) 259.
[10] W. Shi, N. Imaishi, Hydrothermal waves in differentially heated shallow annular pools of silicone oil, J. Cryst. Growth 290 (2006) 280–291, doi:10.1016/j.jcrysgro.2005.12.113.
[11] H. Liu, Z. Zeng, L. Yin, Z. Qiu, L. Qiao, Volume effect on the instabilities of thermocapillary flow in annular pools filled with silicon melt, Int. Commun. Heat Mass Transfer 121 (2021) 105099, doi:10.1016/j.icheatmasstransfer.2020.105099.

[12] J.P. Gollub, S.V. Benson, Many routes to turbulent convection, J. Fluid Mech. 100 (1980) 449, doi:10.1017/S0022112080001243.
[13] E. Bucchignani, D. Mansutti, Horizontal thermocapillary convection of succinonitrile: steady state, instabilities, and transition to chaos, Phys. Rev. E Statistical Nonlinear Soft Matter Phys. 69 (2004) 056319, doi:10.1103/PhysRevE.69.056319.
[14] K. Li, B. Xun, W.R. Hu, Some bifurcation routes to chaos of thermocapillary convection in two-dimensional liquid layers of finite extent, Phys. Fluids 28 (2016) 054106.
[15] L. Zhang, Y.R. Li, C.M. Wu, Q.S. Liu, Flow bifurcation routes to chaos of thermocapillary convection for low Prandtl number fluid in shallow annular pool with surface heat dissipation, Int. J. Therm. Sci. 125 (2018) 23–33.
[16] J. Wang, Z. Guo, C. Jing, L. Duan, K. Li, W. Hu, Effect of volume ratio on thermocapillary convection in annular liquid pools in space, Int. J. Therm. Sci. 179 (2022) 107707, doi:10.1016/j.ijthermalsci.2022.107707.
[17] C. Jing, T. Tsukada, M. Hozawa, K. Shimamura, N. Ichinose, T. Shishido, Numerical studies of wave pattern in an oxide melt in the Czochralski crystal growth, J. Cryst. Growth. 265 (2004) 505–517.
[18] B. Basu, S. Enger, M. Breuer, F. Durst, Three-dimensional simulation of flow and thermal field in a Czochralski melt using a block-structured finite-volume method, J. Cryst. Growth. 219 (2000) 123–143, doi:10.1016/S0022-0248(00)00591-1.
[19] S. Sankaranarayanan, M.L. Spaulding, Dispersion and stability analyses of the linearized two-dimensional shallow water equations in boundary-fitted co-ordinates, Int. J. Numer. Meth. Fluids. 42 (2003) 741–763.
[20] C. Rhie, W.L. Chow, Numerical study of the turbulent flow past an airfoil with trailing edge separation, AIAA J. 21 (1983) 1525–1532.
[21] B. Leonard, The QUICK algorithm-A uniformly third-order finite-difference method for highly convective flows, Comput. Methods Fluids (1980) 159–195.
[22] S.V. Patankar, Numerical Heat Transfer and Fluid Flow, Hemisphere Publishing Corp., Washington, DC, 1980.
[23] C. Jing, S. Ihara, K.-I. Sugioka, T. Tsukada, M. Kobayashi, Global analysis of heat transfer in CZ crystal growth of oxide taking into account three-dimensional unsteady melt convection: effect of meniscus shape, J. Cryst. Growth. 310 (2008) 204–213.
[24] J.N. Kutz, S.L. Brunton, B.W. Brunton, J.L. Proctor, Dynamic Mode Decomposition: Data-Driven Modeling of Complex Systems, Society for Industrial and Applied Mathematics, Philadelphia, PA, 2016, doi:10.1137/1.9781611974508.
[25] P.J. Schmid, Dynamic mode decomposition of numerical and experimental data, J. Fluid Mech. 656 (2010) 5–28, doi:10.1017/S0022112010001217.
[26] N. Demo, M. Tezzele, G. Rozza, PyDMD: python dynamic mode decomposition, JOSS 3 (2018) 530, doi:10.21105/joss.00530.
[27] P.J. Schmid, L. Li, M.P. Juniper, O. Pust, Applications of the dynamic mode decomposition, Theor. Comput. Fluid Dyn. 25 (2011) 249–259, doi:10.1007/s00162-010-0203-9.